Molecular evidence for feedstock-dependent nucleation mechanisms of CNTs

Molecular evidence for feedstock-dependent nucleation mechanisms of CNTs

Umedjon Khalilov*, Charlotte Vets and Erik C. Neyts

PLASMANT research group, Department of Chemistry, University of Antwerp
Universiteitsplein 1, 2610 Antwerpen, Belgium
*e-mail: umedjon.khalilov@uantwerpen.be
phone: +32-3-265.23.82
fax: +32-3-265.23.43

Atomic scale simulations have been shown to be a powerful tool for elucidating the growth mechanisms of carbon nanotubes. The growth picture is however not entirely clear yet due to the gap between current simulations and real experiments. We here simulate for the first time the nucleation and subsequent growth of single-wall carbon nanotubes (SWNTs) from oxygen-containing hydrocarbon feedstocks using the hybrid Molecular Dynamics / Monte Carlo technique. The underlying nucleation mechanisms of Ni-catalysed SWNT growth are discussed in detail. Specifically, we find that as a function of the feedstock different carbon fractions may emerge as the main growth species, due to a competition between the feedstock decomposition, its rehydroxylation and its contribution to etching of the growing SWNT. This study provides a further understanding of the feedstock effects in SWNT growth in comparison with available experimental evidences as well as with *ab-initio* and other simulation data, thereby reducing the simulation-experiment gap.

Introduction

Carbon nanotubes (CNTs) have attracted the attention of many researchers for several decades, thanks to their geometry-dependent electronic, mechanical and optical properties [1]. Among the various synthesis techniques, chemical vapour deposition (CVD) is an often preferred technique due to its simplicity, high degree of control and scalability [2]. In spite of tremendous efforts, the synthesis of nanotubes with controlled properties can be achieved in the CVD process only to some extent, at least in part due to our current incomplete understanding of the growth mechanism [2, 3].

Probably the most sought-after property is chirality-controlled growth. It is often believed that control over the nucleation stage eventually also allows controlling of the CNT chirality [4]. To support this, some transmission electron microscopy (TEM) studies have shown time-resolved details of metal catalysed single-wall CNT (SWNT) nucleation and consequent growth at the atomic level [5, 6]. However, the atomic scale dynamics of the CNT nucleation processes cannot be captured by current TEM resolution [3, 6]. Consequently, a variety of computational techniques have been applied to gain complementary information on various effects, including the importance of the carbon chemical potential [7] or the metal-mediated defect healing [8], the necessity of a carbide phase[9], the influence of C_x growth feedstock [10, 11], and all have contributed to unravelling and explaining experimental observations. In particular, the dislocation theory of chirality-controlled nanotube growth, proposed by Ding and co-workers [12], successfully addresses the growth rate-chiral angle proportionality [13], and the axial rotation of SWNTs [14]. In this kinetic approach, however, the main issue of debate is the neglect of the role of the catalyst nanoparticle, the substrate, the feedstock pressure, and temperature on the resulting (n,m) distribution of grown SWNTs [15-20].

Besides these important factors in CVD-based CNT growth, the choice of the carbon feedstock is one of the main parameters for tuning the SWNT diameter [15-17] and chirality [18-20]. However, real growth species, including hydrocarbon and non-carbon species such as hydrogen, oxygen, and hydroxyl radicals are generally not taken into account in computer simulations, and it is still a major issue [2]. Only very recently, the first dynamic simulation study on the SWNT nucleation using hydrocarbons as a carbon source has been reported, investigating the decomposition of the hydrocarbon molecule [21], the appearance of carbon chains and networks [22, 23] and the formation of a carbon cap [24] on the transition metal nanoparticle surface. These investigations revealed that the dual role of hydrogen and thus the competition between (re)hydrogenation and dehydrogenation processes during the incubation

stage are critical for the dynamics of the SWNT nucleation process [24]. Besides hydrocarbons, oxygen-containing hydrocarbon ($C_xH_yO_z$) feedstocks are also widely used in SWNT growth and thus understanding the role of oxygen is also very important [25-27]. To this end, Oguri and co-workers have very recently studied the decomposition of ethanol molecules on a Ni catalyst surface [28,29]. Although such investigations are quite interesting and give useful information on the onset of SWNT nucleation, understanding the whole picture of SWNT nucleation and growth from $C_xH_yO_z$ species, however, still remains unclear. In this work, we report on carbon nanotube cap nucleation and consequent SWNT growth using different $C_xH_yO_z$ feedstocks through combined reactive Molecular Dynamics and time-stamped force-bias Monte Carlo (MD/tfMC) simulations [8, 24], for the first time. In particular, we found that the competition between catalytic dissociation of $C_xH_yO_z$ feedstock and its hydroxylation and subsequent its etching process is critical in determining the main carbon contributors for SWNT growth.

Computational methodology

MD/tfMC simulation technique. Simulation of the Ni-catalysed SWNT growth from $C_xH_yO_z$ species is performed using a combined reactive MD and tfMC technique [8, 24]. In MD/tfMC, the impacts of the growth species on the nanocatalyst surface and the initial chemical reactions taking place during the first few picoseconds is accounted for by the MD module [24], while the tfMC module subsequently takes care of the longer time relaxation of the system after each chemical reaction. While the exact system dynamics are not reproduced in tfMC calculations, it provides a realistic (albeit not exact) dynamical path, and reproduces end configurations in full agreement with (very long) MD simulations [8].

ReaxFF. In order to properly describe the bond dissociation and formation processes, including the C-C bond dissociation, H_2 or H_2O formation and other reactions during both the MD and the tfMC cycles, the ReaxFF potential [30] is applied with new force-field parameters developed by Zou et al. [31]. To validate the force-field quality, we evaluated test simulations carried out using new parametrized ReaxFF (ReaxFF-Zou) against results obtained using parameterization by Mueller et al. (ReaxFF-Mueller) [32], and other simulations and experimental data [33-39], which are shown in Table 1.

Table 1. Comparison of some results of ReaxFF, other simulations, and experiment

	ReaxFF		Other simulation methods	Experiment
	Zou	Mueller		
E_{coh} (Ni), eV	-4.45	-4.50	-4.42 [35]	-4.44 [36]
ΔH (C), eV	0.62[a] 0.29[b]	0.78[a] 0.68[c]	0.20-0.36 [37] 0.40 [38]	0.42-0.49 [37]
V^F (Ni_xC)/Ω_0	0.78[a]	0.68[a] 0.71[c]	0.64-0.97[c] [37]	--
E_{des} (H_2), eV	1.22[b]	1.66 [39]	0.42-1.19[d]	1.2-1.3[e] [34]

[a] for $Ni_{864}C$ [b] for $Ni_{55}C$ [c] for $Ni_{32}C$ [d] for Ni(100), Ni(110) and Ni(111) [33] [e] for T>500 K [34]

In particular, the ReaxFF-Zou reproduces the cohesive energy of nickel (-4.45 eV) in excellent agreement with experiment (-4.44 eV) [35] as well as DFT calculations (-4.42 eV) [36], while the ReaxFF-Mueller result is somewhat off (-4.50 eV). While the heat of solution of C atom in Ni_{864} bulk (0.62 eV) is slightly higher than the experimental value of about 0.42-0.49 eV [37], the value for the Ni_{55} nanocluster (0.29 eV) is in the range of both experimental and other simulation results (0.2-0.4 eV) [37, 38]. The formation volume V^F quantifies the deformation of the Ni crystal upon incorporation of C in the lattice (Ni_xC). It is defined as $V^F = V(Ni_xC) - x\Omega_0(Ni)$, where $V(Ni_xC)$ and $\Omega_0(Ni)$ are the volume of the relaxed Ni_xC structure and the volume per atom of elemental Ni, respectively, where x is the number of Ni atoms in the system. We found that the V^F/Ω_0 ratio (0.78) is in close agreement with the *ab-initio* data of Siegel et al. (0.64-0.8) [37], although the value is slightly higher than the value calculated using the ReaxFF-Mueller parametrization (0.68 and 0.71 for $Ni_{864}C$ and $Ni_{32}C$, respectively). Also, we calculated the energy barrier of H_2 desorption from the Ni surface to be 1.22 eV, which is close to the range of DFT calculation results (0.42-1.19 eV) [33] and in very close agreement with the experimental activation energy (1.2 - 1.3 eV) [34], while the ReaxFF-Mueller parametrization yields a slightly too high value (1.66 eV) [39]. In spite of quantitative differences between ReaxFF-Mueller and ReaxFF-Zou results, our test simulations indicate that such small differences do not affect the overall growth mechanisms (see Fig. 1 in the Supplementary information). The overall results indicate the new ReaxFF potential is sufficiently accurate to address catalysed CNT growth using MD/tfMC simulations.

Simulation details. For the simulation of SWNT growth, a Ni_{55} nanocluster is initially equilibrated at 2000 K using the canonical Bussi thermostat [40]. The nanocatalyst is

physisorbed on a virtual Al surface, employing a *z*-integrated Lennard-Jones potential [23]. In order to gain a generic understanding of the role of $C_xH_yO_z$ feedstocks, we use three different molecules, *viz.* formaldehyde (CH_2O) and ethanol (C_2H_6O) molecules, which have double or single C-C bonds, respectively, and complex β-methyl lactoside ($C_{13}H_{24}O_{11}$) molecule (Fig. 1).

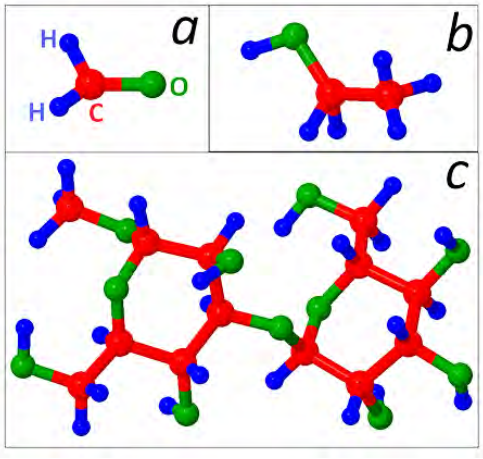

Figure 1. Ball-stick model of the three $C_xH_yO_z$ feedstocks, *i.e.*, (*a*) formaldehyde, (*b*) ethanol and (*c*) β-methyl lactoside molecules. C, H and O atoms are shown in red, blue and green colours, respectively.

The molecules are allowed to impinge on the cluster one by one, while keeping their number density in the simulation cell constant during the simulations. Due to lower pyrolysis temperature of the $C_{13}H_{24}O_{11}$ (~ 445 K) [41] and C_2H_6O (1050-1275 K) [42] molecules, comparing to CH_2O (2200-2650 K) [43], different molecular fractions can already be found in the gas-phase before the molecule impinges on the catalyst surface at 2000 K. However, we found that the formation rate of the pyrolysis products is very low. When a gas-phase species adsorbs on the nanocluster, the resulting structure is allowed to relax by application of tfMC [23, 24]. During the relaxation, no new feedstock is allowed to enter the simulation cell.

DFT calculations. The VASP software [44] is used for DFT calculations of adsorbed/dissociated/desorbed H_2 and H_2O molecules on/from the Ni_{55} nanocatalyst. Optimizations are done in the generalized gradient approximation (GGA), using the revised Perdew-Burke-Ernzerhof (RPBE) functional [45], and the projector augmented wave method (PAW) [46]. Methfessel-Paxton smearing of the first order is used [47], along with a Γ-centered (1 x 1 x 1) k-point mesh. Supercells with sizes of (20 x 20 x 20) Å are employed, except for the structures where H_2 and H_2O are desorbed from the nanoparticle, in which case the size is (30 x 30 x 30) Å. Spin polarization with no symmetry constraints are employed.

The energy cutoff is set to 500 eV, and the energy convergence to 1 x 10^{-6} eV. A magnetic moment is applied to the Ni atoms.

Results and discussions

From our results we infer that SWNT nucleation and its subsequent growth from $C_xH_yO_z$ feedstocks can be distinguished into three stages, which are similar to SWNT growth from non-oxygen containing hydrocarbon species [24]: (i) incubation, (ii) cap formation and (iii) continued (tube) growth, as illustrated in Fig. 2. We find that the SWNT nucleation from $C_xH_yO_z$ feedstocks is clearly different from both pure carbon (C_x) [7-10, 48] and hydrocarbon (C_xH_y) species [22-24]. However, fast C dissolution after the feedstock dissociation at the onset of incubation stage is identical for all types of growth species.

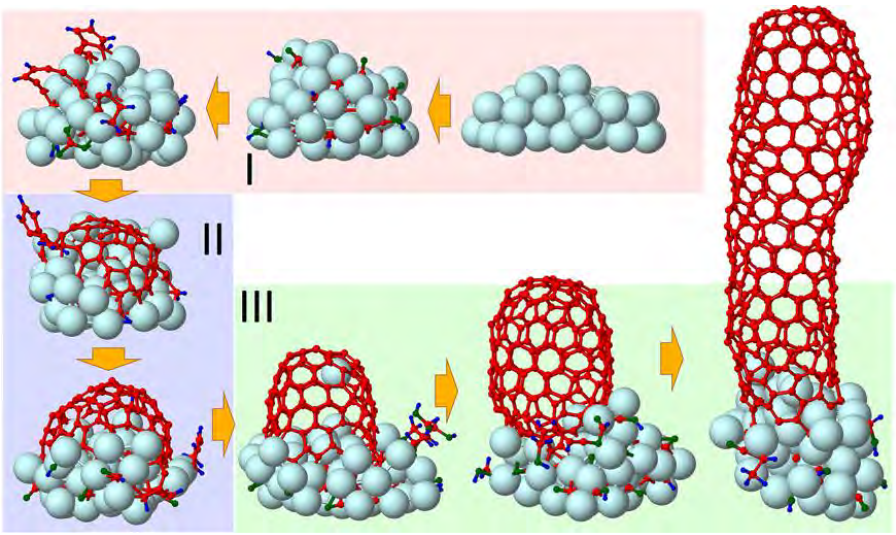

Figure 2. Base-growth process of SWNT from $C_xH_yO_z$ species, divided into three stages. Ni, C, H and O atoms are shown in cyan, red, blue and green colours, respectively.

Feedstock-catalyst reactions. As representative for all $C_xH_yO_z$ feedstocks, we here analyse the entire adsorption/dissolution process of the ethanol (C_2H_6O) molecule on/in a Ni nanocatalyst. After impingement on the cluster, the molecule typically first binds to the surface with its O-atom (Fig. 3*a* and *b*). While the feedstock sticking probability depends on the nature of the Ni facets [33], the Ni nanoparticle is amorphized at high temperature and therefore it does not contain any specific facets during the entire growth process. Consequently, all C-H, C-O and C-C bonds of the molecule are gradually broken (Fig. 3*c-j*). In particular, C–C bonds from the surface CH_xCO fragment (e.g., HCCO in Fig. 3*f*) are

dissociated (Fig. 3*g*) during the simulation, which concurs with previous *ab-initio* MD calculation results [29]. Yet, binding of another H-adatom to the remaining CO fragment leads to weakening and consequently breaking of the single C-O bond (Fig. 3*i* and *j*). In the CH_2O case, however, such H binding is rather rare due to low concentration of H adatoms and consequently CO fragments remain longer on the cluster or desorb from the cluster. After C-O bond breaking, the single C atom quickly dissolves into cluster. During the feedstock dissociation, H adatoms eventually associate with a remaining OH fragment or another H adatom and desorb as a water or a hydrogen molecule from the cluster surface, respectively (Fig. 3*k* and *l*).

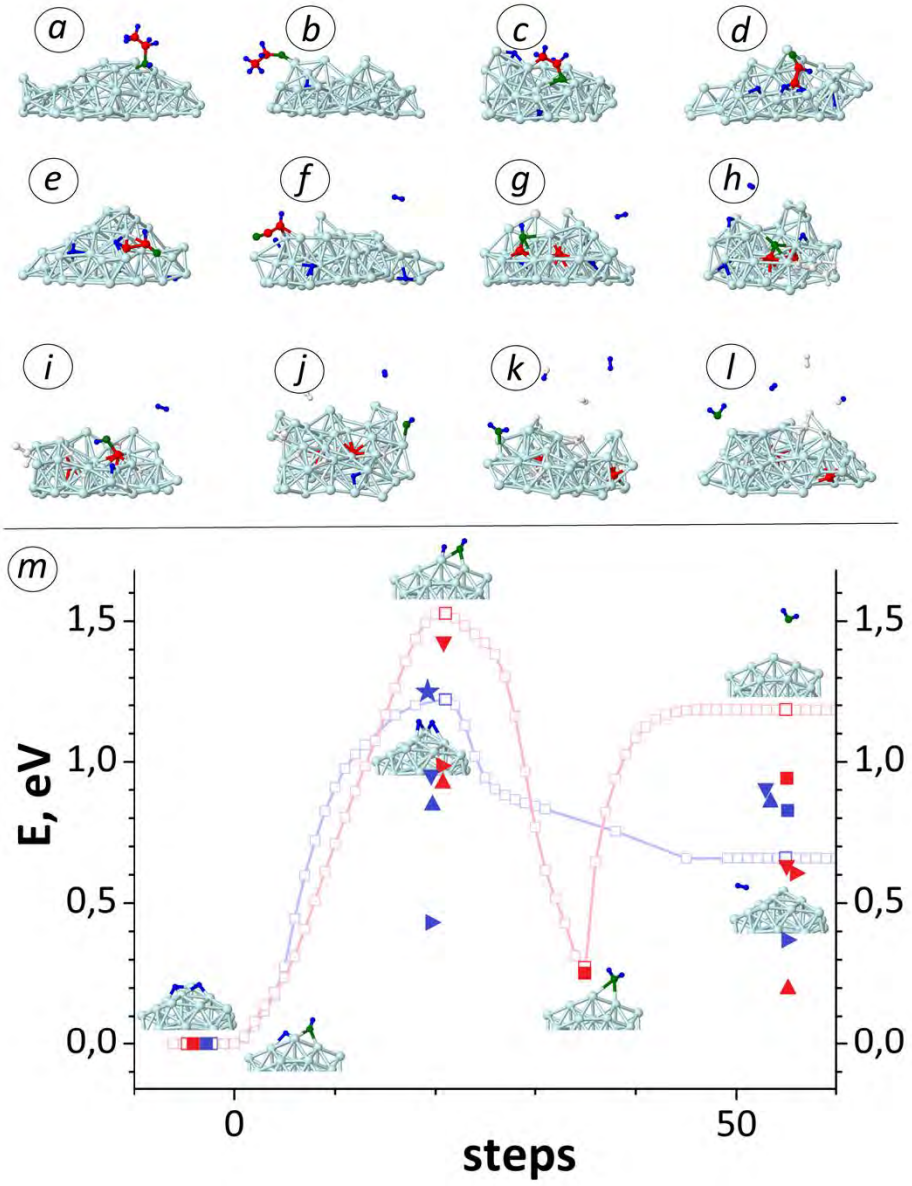

Figure 3. (*a* - *l*) Adsorption and dissociation steps of ethanol molecules on Ni_{55} cluster. The fractions or individual atoms of other adsorbed ethanol molecules are coloured in white, for the sake of clarity. (*m*) Association/dissociation activation barriers in desorption/adsorption of H_2

(blue line with open squares) and H_2O molecules (red line with open squares) on Ni_{55} nanocluster. DFT values for H_2O on Ni(111), on Ni(110) and Ni(100) surfaces [33] are indicated by red up, red down and red right triangles, respectively. DFT data for H_2O on Ni_{55} is indicated by red squares. Also, DFT data for H_2 [33] are shown in blue. Furthermore, the blue star indicates the experimental activation energy barrier for H_2 desorption [34].

Hydrogenation vs oxidation. Employing nudged elastic band (NEB) [49] calculations (Fig. 3*m*), an energy barrier for the recombination of OH and H species on the Ni_{55} cluster is found to be 1.53 eV (red open squares in Fig. 3*m*). This value is a slightly higher than DFT values for different nickel facets, *i.e.*, 0.87 eV for Ni(111), 0.94 eV for Ni(110) and 1.39 eV for Ni(100) surfaces (red up triangles, red right triangles and red down triangles, respectively, in Fig. 3*m*) [33]. These species subsequently desorb as a H_2O molecule from the Ni surface. The same water formation mechanism was also reported in *ab-initio* MD studies [28]. In contrast to the recombination and desorption, H_2O re-adsorption is found to be barrier-less. The adsorbed molecule preferably desorbs again from the surface rather than dissociatively chemisorbing on the catalyst surface: the desorption and splitting barriers are 0.91 eV (our DFT value is 0.71 eV, see red squares in Fig. 3*m*) and 1.25 eV, respectively. Thus, most adsorbed H_2O molecules desorb again without proceeding to decompose to OH + H species, which is in agreement with both experimental [50, 51] and DFT calculation results [52]. As mentioned above, H adatoms freely diffuse over the cluster surface (with a maximum diffusion barrier of 0.51 eV) comparing to adsorbed OH, until it recombines with either an OH specie (1.53 eV) or another H adatom (1.22 eV) in order to desorb as H_2O or H_2 molecule, respectively. Our results show that the OH diffusion barrier is rather high, about 2 times higher than the H diffusion barrier due to its high adsorption (binding) energy, which is in agreement with DFT calculation results [33]. Also, the value for the H_2 desorption energy barrier (blue open squares in Fig. 3*m*) is in close agreement with the experimental activation energy in the range of 1.2-1.3 eV (blue star in Fig. 3*m*) [34] and first-principle results, ranging from 0.42 eV to 1.37 eV for different nickel surfaces (blue triangles in Fig. 3*m*) [33]. While both recombination energy barriers differ somewhat from DFT values, overall DFT and MD/tfMC calculations indicate that the formation rate of OH&H pairs on the cluster surface (*i.e.*, $HO^*+H^*+Ni \rightarrow H_2O\uparrow+Ni$) is relatively slow compared to the H&H formation rate (*i.e.*, $H^*+H^*+Ni \rightarrow H_2\uparrow+Ni$). Furthermore, the positive reaction energies of 0.66 eV for H_2 and 1.18 eV for H_2O are close to first-principle values in the range 0.36-0.90 eV for H_2 (blue triangles and squares) and 0.20-0.94 eV for H_2O (red triangles and squares) [33], indicating the

endergonic nature of both H_2 and H_2O desorption reactions. Therefore, both desorbed molecules preferable re-adsorb again on the catalyst surface. While the H_2 adsorption barrier is non-zero (0.24 eV) unlike H_2O adsorption, the chemical dissociation barrier of the H_2 molecule (0.56 eV) is much lower than the dissociation barrier of the H_2O molecule (1.25 eV). Comparing dissociative adsorption and associative desorption probabilities of H_2 and H_2O molecules, the results point out that the probability for hydrogenation is higher than for oxidation during the CNT growth from $C_xH_yO_z$ species. In addition, the high non-dissociative adsorption rate of H_2O due to its zero-barrier can assist in the growth of defect-less SWNT [25].

Super-saturation point. When a $C_xH_yO_z$ molecule completely dissociates, all C atoms are found as dissolved species in Ni_{55} nanocluster, which is similar to simulation studies of SWNT nucleation from C_x [7-10, 48] and C_xH_y species [22-24] at the SWNT nucleation onset. This scenario of "$C_xH_yO_z$ adsorption/dissociation, C dissolution, as well as H_2 and H_2O desorption" continues until the nanocluster is saturated, *i.e.*, no space is available in the catalyst. At this supersaturation point (indicated by the dashed line in Fig. 4*a*) [48], the number of dissolved C atoms can gradually increase up to about 30% of the amount of Ni atoms (Fig. 4*a*, dissolved C). After supersaturation, the amount of dissolved C atoms reduces through the formation different carbon species and subsequent incipient carbon nanostructures on the catalyst surface.

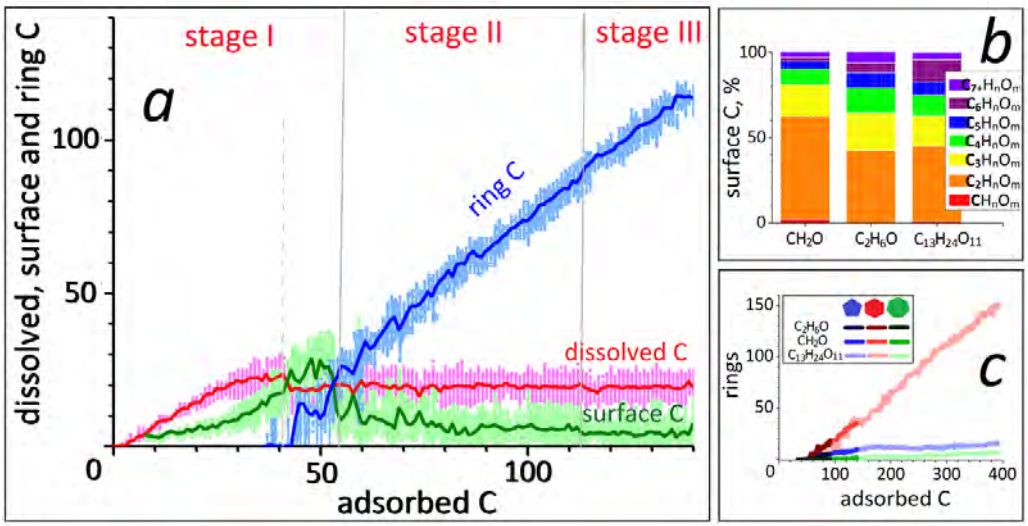

Figure 4. (*a*) Distribution of adsorbed C atoms as function of its total number during SWNT growth from CH_2O molecules: number of dissolved C atoms, surface C atoms and ring-related C atoms. (*b*) Relative fractions of surface C species ($C_kH_nO_m$) during the SWNT

nucleation/growth from CH_2O, C_2H_6O and $C_{13}H_{24}O_{11}$ molecules. (*c*) Evolution of the number of pentagons, hexagons and heptagons as a function of the number of C adatoms during the growth from CH_2O, C_2H_6O and $C_{13}H_{24}O_{11}$ molecules.

Surface carbon species. The appearance of surface C species can be explained by the decreasing catalyst activity after its saturation. As a result, feedstock fractions preferably remain at and diffuse over the catalyst surface rather than splitting and diffusing into the catalyst [10]. The results indicate that surface carbon species are the product of the competition between the feedstock dissociation due to the saturated catalyst and its re-hydroxylation/etching caused by non-carbon surface species such as H, O and OH. Because of this competition, the number of remaining $C_kH_nO_m$ species increases on decreasing their carbon content, as shown in Fig. 4*b*. Consequently, $C_2H_nO_m$ species, including carbon dimers, are the predominant species found among all surface species in all feedstock cases, which is in agreement with the theoretical suggestions [11, 53]. Recent first-principle calculation results lead to the conclusion that chiral selective CNTs can elongate through the addition of C_2-fragments instead of adding C atoms one-by-one and the incorporation of C_2 species into the SWNT rim continues the growth without changing its chirality [11, 53]. Furthermore, $C_6H_nO_m$ species, including C_6 polyyne chains, increases when the growth feedstock contains more carbon atoms. The appearance of such six-atom chains eventually leads to hexagon formation on the catalyst surface, hence the fast network elongation. When incipient carbon rings, *e.g.*, pentagons or hexagons, appear on the surface, the number of surface C species considerably decreases (Fig. 4*a*). While their amount fluctuates around a constant number in stage II, it gradually lowers in the final growth stage due to the blocking of most of the available area on the catalyst surface by the growing tube (Fig. 4*c*).

Desorption vs etching. While the supply probability of surface C species to the growing carbon network is obviously very high after the supersaturation point, the contribution of desorbed or etched gas-phase species to the growth process is not negligible. In Fig. 5, desorbed and etched species, *i.e.*, gas-phase non-C and C species are analysed. In particular, the number of desorbed H_mO_n species, including water and hydrogen molecules, is relatively high, *i.e.*, it corresponds to about 70% of all desorbed species for all three cases (Fig. 5*b*).

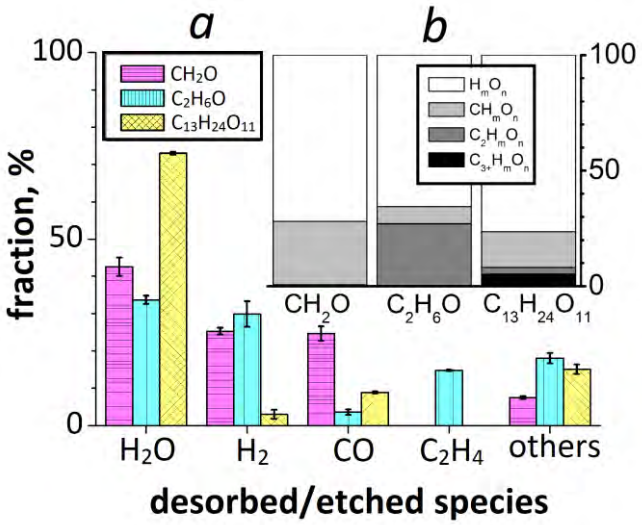

Figure 5. (*a*) Fractions of most common desorbed and etched species as well as (*b*) fractions of desorbed non-carbon (*i.e.*, H_mO_n) and etched carbon species (*i.e.*, CH_mO_n, $C_2H_mO_n$ and $C_{3+}H_mO_n$) during SWNT growth from $C_xH_yO_z$ molecules.

We find that desorption of H_2O and H_2 is favourable for all cases (Fig. 5*a*). From the NEB calculations presented in the previous sections, we find that adsorbed H_2 molecules easily split to H adatoms due to the low dissociation energy barrier, whereas adsorbed H_2O molecules prefer to desorb again rather than dissociate to OH and H surface species [50-52]. Consequently, the concentration of desorbed H_2O molecules increases in comparison to the concentration of desorbed H_2 molecules. H adatoms originating from splitting H_2 molecules may lead to etching of a growing cap/tube [54, 55], in addition to their contributions to the etching process of surface carbon species. Also, H_2O dissociative adsorption may contribute to removal of amorphous carbon from the cluster, improving defect-less tube growth [25, 26]. However, we do not observe SWNT oxidation and subsequent SWNT damage caused by adsorbing H_2O, which is again in agreement with earlier experimental evidence [25].

Besides non-carbon species, re-adsorption of etched carbon species (about 30% of all gas-phase species in Fig. 5*b*) can be responsible for two effects, *i.e.*, (1) enhancing the tube growth or (2) increasing topological defects or additional structures on the grown tube [56, 57]. Fig. 4*a* shows that desorption of carbon monoxide occurs in all feedstock cases, whereas desorption of ethylene molecules is only found in the ethanol-assisted SWNT growth. Here, the high desorption rate of CO and C_2H_4 molecules in the CH_2O and C_2H_6O cases, respectively, can be explained by the existence of the strong carbonyl (C=O) group in formaldehyde and the much weaker C-O linkage in ethanol molecules, respectively. The results show that the total amount of other etched species is also not minor, although their

partial concentration is negligible: the ratio of $CH_mO_n/C_2H_mO_n/C_{3+}H_mO_n$ desorbed species is about 27/1/0, 8/27/0 and 16/3/5 (in %) for the CH_2O, C_2H_6O and $C_{13}H_{24}O_{11}$ cases, respectively (Fig. 5*b*). Thus, the analysis of all carbon-containing species clarifies which etched carbon species have a high probability to contribute to SWNT nucleation and growth from $C_xH_yO_z$ feedstocks.

Carbon contributors. We find three types of species contributing to the growing tube, *i.e.*, surface carbon species, dissolved carbon atoms and gas-phase (previously etched) carbon species, as shown in Fig. 6*a*.

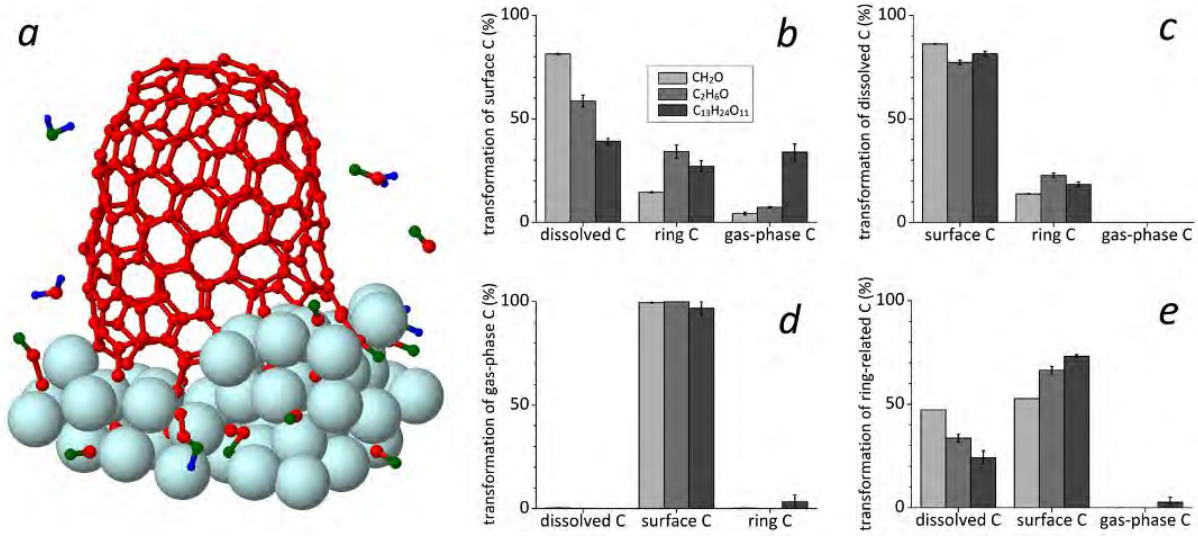

Figure 6. (*a*) Three types of carbon contributors during SWNT growth. Transformation of (*b*) surface carbon species, (*c*) dissolved carbon atoms, (*d*) gas-phase (etched) carbon species and (*e*) ring-related carbon atoms to other carbon species. Each bar is an average of two (short and long relaxation after each reaction) simulation runs for the same feedstock.

These contributors can directly transform to ring-related carbon atoms through their incorporation into the tube rim. Also, ring-C atoms can transform to these contributors again. Overall, these four carbon species can transform to other species during the growth process. In particular, surface C species subsequently convert or transform to all other carbon species, *i.e.*, dissolved, ring- and gas-phase C species, as function of the feedstock type (Fig. 6*b*). The conversion to the dissolved and gas-phase species depends on the carbon index in the feedstock. In particular, the transformation to dissolved C atom increases with decreasing amount of C in the feedstock and this phenomenon can be explain by the dissociation/etching rate of the feedstock or/and its fraction(s). In contrast, the conversion to gas-phase C species

increases with increasing carbon amount in the feedstock. This phenomenon can be explained by the high re-hydroxylation and etching rates of the precursor(s). Obviously, both conversion/transformation rates indicate that there is a competition between hydroxylation/etching of the remaining fraction(s) due to hydrogen/oxygen adatoms and dissociation/dissolution of the fraction(s) due to the catalyst. Also, the incorporation of both surface (Fig. 6*b*) and dissolved C species (Fig. 6*c*) to the carbon network or to the tube-end is related to the feedstock type, while these contributors mainly transform to each other. However, nearly all gas-phase (etched) carbon species transform to surface C species for all feedstock cases (Fig. 6*d*). Also, the transformation of ring-C to surface C species is significant, although its contribution to dissolved C is also not negligible (Fig. 6*e*). Both transformations strongly depend on the amount of carbon atoms in the feedstock. Obviously, the surface C species are overall the main contributors to the CNT growth for all three $C_xH_yO_z$ feedstocks (see Table 1 in the Supplementary Information). Regarding DFT calculation results [11], we also suggest that dissolved carbon atoms (C_1) favour change the SWNT chirality, while surface C species (C_n) result in both chirality change and growth.

Despite the huge number of C-C association and dissociation reactions in the tube-catalyst interface, the amount of C atoms in the grown network linearly rises during the SWNT nucleation/growth (Fig. 4*a,* ring C). In the carbon network, the number of hexagons continuously increases, while the formation of pentagons and heptagons initially speeds up and subsequently their number remains constant during the growth (Fig. 4*c*). While the ring formation rates per adsorbed C atom for all feedstock cases are identical, the formation rate depends on the C sticking/incorporation rate (see Figure 3*b* in the Supplementary Information). Consequently, a high rate of hexagon formation due to carefully chosen feedstock assures the growth of a less-defective tube with a certain diameter [58].

Tube diameter vs feedstock. We compare the effect of small (CH_2O) and large ($C_{13}H_{24}O_{11}$) feedstock molecules, which contain a similar C/H/O ratio (~1/2/1), resulting in two growth modes: “tangential”, when tube and nanoparticle diameters are identical ($d_{CNT}/d_{NP}\approx1$) (Fig. 7*b*), and “perpendicular”, when the tube diameter is smaller than the nanoparticle diameter ($d_{CNT}/d_{NP}<0.8$) (Fig. 7*c* and *d*), respectively.

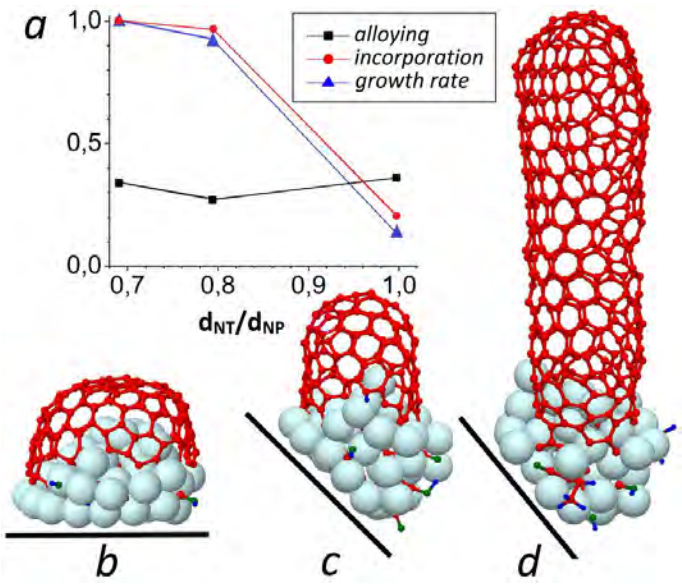

Figure 7. (*a*) Dependence of the alloying of the Ni nanoparticle with dissolved C atoms (black lines with squares), the incorporation rate of C contributors to SWNT rim (red lines with circles) and the growth rate of SWNT (blue lines with triangles) on the diameter ratio between nanoparticle (nanocatalyst) and tube (d_{NT}/d_{NP}), grown from (*b*) CH_2O and (*c* and *d*) $C_{13}H_{24}O_{11}$ feedstocks. The values of incorporation and growth rate are normalized. The first (*b*) and second (*c*) tubes both contain about 120 C atoms. The third tube (*d*) is an extended version of the second tube, which consists of about 360 C atoms. The black line indicates the surface of the virtual Al substrate.

This feedstock effect was already reported by He and co-workers [16]. In their study, Fe-catalysed-SWNTs with narrow diameter were produced by using CO as the carbon source, while large-diameter SWNTs were produced by using CH_4. They explained that CO based growth leads to a high amount of dissolved carbon, resulting in a tube that is narrower than the nanoparticle diameter, while CH_4 yields less dissolved C in the nanoparticle and a large diameter tube [59]. In our results, the tube-nanoparticle ratio, however, seems not to significantly depend on the concentration of dissolved C into the liquefied nanoparticle, as shown in Fig. 7*a*. Instead, the figure clearly indicates that the C incorporation and the tube elongation (growth) rates are significantly changed when the d_{CNT}/d_{NP} ratio alters. While both feedstocks have the same C/H/O ratio, the carbon supply of the large feedstock allows a high C incorporation and thus results in fast tube growth with a narrow-diameter. In contrast, under low C incorporation, the wide-diameter tube grows slowly. Such growth behaviour is in agreement with recent *in situ* TEM observations. Zhang *et al*. observed a change of SWNT diameter as a function of the ratio between carbon supply (C_{supply}) and carbon incorporation (C_{inc}) rates and they found that necking and broadening of SWNTs occurs when $C_{supply}/C_{inc}<1$

and $C_{supply}/C_{inc}>1$, respectively [60]. In particular, they proposed two reasons for necking and subsequent the cessation of SWNT, *i.e.*, insufficient active carbon species (or fast carbon incorporation) and a certain amount of stress exerted at the tube-catalyst interface. Overall, it indicates that fast (or slow) carbon incorporation leads to SWNT growth with a narrow (or wide)-diameter. This explanation completely corroborates our results in Fig. 7*a*: the carbon incorporation rate inversely depends on the d_{NT}/d_{NP} ratio. Besides in the $C_xH_yO_z$ case, this phenomenon is also observed in both C_x and C_xH_y feedstock cases (see Fig. 2 and 3 in the Supplementary information).

We also find that the incorporation of hydrogen or oxygen adatoms into the grown tube leads to an increase or reduction of the tube diameter. In particular, reactive hydrogen atoms can quickly impinge on a carbon sheet or a cap-end and reduce the sheet/cap-catalyst adhesion. Consequently, the carbon cap expands over the surface by shrinking its rim diameter such that the carbon sheet can partially cover the catalyst surface. Our previous studies revealed that such carbon nanosheets can even transform to free-standing single or parallel carbon sheets at low growth temperatures due to high H and lower C concentrations [23, 24]. The appearance of such parallel carbon nanowalls [23] may explain the nucleation onset of multi-walled CNT (MWNT) [24], as earlier proposed by Hofmann and co-workers [5]. On the other hand, such transformations are less frequent in $C_xH_yO_z$ based SWNT growth due to the oxygen scavenging of reactive hydrogen atoms [27]. As a result, the nucleation probability of CNTs with a low-wall-number or a narrow-diameter increases during the $C_xH_yO_z$-based growth [20, 27]. This suggestion is supported by an experimental observation of the Fe-catalysed SWNT and double-walled CNT (DWNT) growth from $C_xH_yO_z$ and C_xH_y feedstocks [20]. In particular, they found SWNT/DWNT population yields (in %) of about 92/8, 89/11 and 25/75 for ethanol (C_2H_6O), toluene (C_7H_8) and methane (CH_4)-based CNT growth, respectively. Such a yield sequence is also compatible with the sequence of pyrolysis temperatures of these molecules, which are ~1025 K, ~1050 K and ~1470 K, respectively. Our calculation results also agree with this evidence: a large ($C_{13}H_{24}O_{11}$) feedstock with a low pyrolysis temperature (~445 K) yields narrow-diameter tubes (perpendicular mode) and a small (CH_2O) feedstock with high pyrolysis temperature (2200-2650 K) results in large-diameter tubes (tangential mode). This indicates that the fast decomposition increases the carbon concentration and thus its incorporation rate. On the other hand, Wang and co-workers grew narrow- and wide-diameter tubes by CO and C_2H_2 feedstocks, respectively, while the decomposition rate of C_2H_2 is much higher than that of CO [15]. They thus concluded that the feedstock pressure is

a key factor to chirality (diameter) control. Also, Lu *et al*. found that diameters of SWNTs were closely related to the carbon feeding rate by selective activation of nanoparticles [19].
In general, from our calculation results and available theoretical and experimental evidence [11, 15-20, 27, 59, 60], we conclude that the tube diameter can be controlled by the incorporation rate of the aforementioned three carbon contributors. Besides the choice of catalyst, temperature and pressure, the choice of feedstock and associated growth precursors allows tuning the formation of desirable carbon contributors due to competition between alloying catalysts and non-carbon etchant species, which can eventually steer the diameter and possibly chirality of SWNTs.

Conclusion

The nucleation of incipient SWNTs from oxygen-containing hydrocarbon feedstocks is computationally studied for the first time. All simulation results are obtained using a combined MD/tfMC simulation technique. The overall results indicate that if we can control the formation of three main carbon contributors, *i.e*., dissolved C atoms, surface C species and gas-phase (etched) C species, we can control the carbon incorporation into the rim of the growing cap/tube. Our results show that the appearance of these contributors is due to catalyst and etchant species, which result either completely or partially from the dissociation of the carbon feedstock. Therefore, the choice of the growth feedstock determines the competition between these processes, and allows preferable carbon species to be selectively incorporated into a growing tube, contributing to controlled SWNT quality (defect density) and radius.

Acknowledgements

The authors gratefully acknowledge financial support from the Research Foundation - Flanders (FWO), Belgium (Grant numbers 12M1318N and 1S22516N). The work was carried out in part using the CalcUA core facility of the Universiteit Antwerpen, a division of the Flemish Supercomputer Centre VSC, funded by FWO and the Flemish Government (Department EWI). We thank Prof. A. C. T. van Duin for sharing the reax-code and force-field parameters.

References

1. Iijima, S. Helical microtubules of graphitic carbon. *Nature* **354**, 56-58 (1991).
2. Jourdain, V. & Bichara, C. Current understanding of the growth of carbon nanotubes in catalytic chemical vapour deposition. *Carbon* **58,** 2-39 (2013).
3. Tessonnier, J. -P. & Su, D. S. Recent Progress on the Growth Mechanism of Carbon Nanotubes: A Review. *ChemSuSChem* **4,** 824-847 (2011).
4. Reich S., Li L. & Robertson J. Structure and formation energy of carbon nanotube caps. *Phys. Rev. B* **72**, 165423 (2005).
5. Hofmann, S. *et al.* In situ Observations of Catalyst Dynamics during Surface-Bound Carbon Nanotube Nucleation. *Nano Lett.* **7,** 602-608 (2007).
6. Yoshida, H., Takeda, S., Uchiyama, T., Kohno, H. & Homma, Y. Atomic-Scale In-situ Observation of Carbon Nanotube Growth from Solid State Iron Carbide Nanoparticles. *Nano Lett.* **8,** 2082-2086 (2008).
7. Amara, H., Bichara, C. & Ducastelle, F. Understanding the nucleation mechanisms of carbon nanotubes in catalytic chemical vapor deposition. *Phys. Rev. Lett*. **100,** 056105 (2008).
8. Neyts, E. C., Shibuta, Y., van Duin, A. C. T. & Bogaerts, A. Catalyzed Growth of Carbon Nanotube with Definable Chirality by Hybrid Molecular Dynamics Force Biased Monte Carlo Simulations. *ASC Nano* **4,** 6665-6672 (2010).
9. Page, A. J., Yamane, H., Ohta, Y., Irle, S. & Morokuma, K. QM/MD Simulation of SWNT Nucleation on Transition-Metal Carbide Nanoparticles. *J. Am. Chem. Soc.* **132,** 15699–15707 (2010).
10. Gómez-Gualdrón, D. A., Beetge, J. M., Burgos, J. C. & Balbuena, P. B. Effects of Precursor Type on the CVD Growth of Single-Walled Carbon Nanotubes. *J. Phys. Chem. C* **117,** 10397–10409 (2013).
11. Wang, Q., Ng, M.-F., Yang, S.-W., Yang, Y. & Chen, Y. The Mechanism of Single-Walled Carbon Nanotube Growth and Chirality Selection Induced by Carbon Atom and Dimer Addition. *ACS Nano* **4**, 939-946 (2010).
12. Ding, F., Harutyunyan, A. & Yakobson, B. I. Disslocation theory of chirality-controlled nanotube growth. *PNAS* **106**, 2506-2509 (2009).
13. Rao, R., Liptak, D., Cherukuri, T., Yakobson, B. I. & Maruyama, B. *In situ* evidence for chirality-dependent growth rates of individual carbon nanotubes. *Nature Materials* **11**, 213-216 (2012).

14. Marchand, M., Journet, C., Guillot, D., Benoit, J.-M., Yakobson, B. I. & Purcell, S. T. Growing a Carbon Nanotube Atom by Atom: “And Yet It Does Turn”. *Nano Lett*. **9**, 2961-2966 (2009).
15. Wang, B., Poa, C. H. P., Wei, L., Li, L.-J., Yang, Y. & Chen, Y. (n,m) Selectivity of Single-Walled Carbon Nanotubes by Different Carbon Precursors on Co−Mo Catalysts. *J. Am. Chem. Soc.* **129**, 9014-9019 (2007).
16. He, M., Jiang, H., Kauppinen, E. I. & Lehtonen, J. Diameter and chiral angle distribution dependencies on the carbon precursors in surface-grown single-walled carbon nanotubes *Nanoscale* **4**, 7394 (2012).
17. Loebick, C. Z., et al. Selective Synthesis of Subnanometer Diameter Semiconducting Single-Walled Carbon Nanotubes. *J. Am. Chem. Soc.* **132**, 11125-11131 (2010).
18. Wei, L. *et al*. Narrow-chirality distributed single-walled carbon nanotube synthesis by remote plasma enhanced ethanol deposition on cobalt incorporated MCM-41 catalyst. *Carbon* **66**, 134–143 (2014).
19. Lu, C. & Liu, J. Controlling the Diameter of Carbon Nanotubes in Chemical Vapor Deposition Method by Carbon Feeding. *J. Phys. Chem. B* **110**, 20254-20257 (2006).
20. Barnard, J. S., Paukner, C. & Koziol, K. K. The role of carbon precursor on carbon nanotube chirality in floating catalytic chemical vapour deposition. *Nanoscale* **8**, 17262-17270 (2016).
21. Arifin, R., Shibuta, Y., Shimamura, K., Shimojo, F & Yamaguchi, S. *Ab Initio* Molecular Dynamics Simulation of Ethylene Reaction on Nickel (111) Surface. *Phys. Chem. C* **119,** 3210-3216 (2015).
22. Wang, Y. *et al*. Quantum chemical simulations reveal acetylene-based growth mechanisms in the chemical vapor deposition synthesis of carbon nanotubes. *Carbon* **72,** 22-37 (2014).
23. Khalilov, U., Bogaerts, A. & Neyts, E. C. Microscopic mechanisms of vertical graphene and carbon nanotube cap nucleation from hydrocarbon growth precursors *Nanoscale* **6,** 9206-9214 (2014).
24. Khalilov, U., Bogaerts, A. & Neyts, E. C. Atomic scale simulation of carbon nanotube nucleation from hydrocarbon precursors. *Nat. Commun.* **6** 10306 (2015).
25. Hata, K., Futaba, D. N., Mizuno, K., Namai, T., Yumura, M. & Iijima, S. Water-Assisted Highly Efficient Synthesis of Impurity-Free Single-Walled Carbon Nanotubes. *Science* **306**, 1362-1364 (2004).

26. Maruyama, S., Kojima, R., Miyauchi, Y., Chiashi, S. & Kohno, M. Low-temperature synthesis of high-purity single-walled carbon nanotubes from alcohol. *Chemical Physics Letters* **360**, 229–234 (2002).
27. Zhang, G. et *al.* Ultra-high-yield growth of vertical single-walled carbon nanotubes: Hidden roles of hydrogen and oxygen. *PNAS* **102,** 16141-16145 (2005).
28. Oguri, T., Shimamura, K., Shibuta, Y., Shimojo, F. & Yamaguchi, S. *Ab Initio* Molecular Dynamics Simulation of the Dissociation of Ethanol on a Nickel Cluster: Understanding the Initial Stage of Metal-Catalyzed Growth of Carbon Nanotubes. *J. Phys. Chem. C* **117**, 9983-9990 (2013).
29. Oguri, T., Shimamura, K., Shibuta, Y., Shimojo, F. & Yamaguchi, S. Bond dissociation mechanism of ethanol during carbon nanotube synthesis via alcohol catalytic CVD technique: *Ab initio* molecular dynamics simulation. *Chemical Physics Letters* **595–596**, 185–191 (2014).
30. van Duin, A. C. T., Dasgupta, S., Lorant, F. & Goddard III, W. A. ReaxFF: A Reactive Force Field for Hydrocarbons. *J. Phys. Chem. A* **105,** 9396-9409 (2001).
31. Zou, C., Shin, Y. K., van Duin, A. C. T., Fang, H & Liu, Z.-K. Molecular dynamics simulations of the effects of vacancies on nickel self-diffusion, oxygen diffusion and oxidation initiation in nickel, using the ReaxFF reactive force field. *Acta Materialia* **83**, 102-112 (2015).
32. Mueller, J. E., van Duin, A.C.T. & Goddard III, W. A. Development and Validation of ReaxFF Reactive Force Field for Hydrocarbon Chemistry Catalyzed by Nickel. *J. Phys. Chem. C* **114,** 4939-4949 (2010).
33. Mohsenzadeh, A., Richards, T. & Bolton, K. DFT study of the water gas shift reaction on Ni(111), Ni(100) and Ni(110) surfaces. *Surface Science* **644**, 53-63 (2016) and references therein..
34. Cabrera, A. L. Desorption studies of hydrogen and carbon monoxide from nickel surfaces using thermal desorption spectroscopy. *J. Vac. Sci. Technol. A* **8**, 3229-3236 (1990).
35. Kittel, C. Introduction to Solid State Physics, 8th ed.; Wiley: New York, 2005.
36. Assowe, O., Politano, O., Vignal, V., Arnoux, P., Diawara, B., Verners, O. & van Duin, A. C. T. Reactive Molecular Dynamics of the Initial Oxidation Stages of Ni(111) in Pure Water: Effect of an Applied Electric Field. *J. Phys. Chem. A* **116**, 11796-11805 (2012).
37. Siegel, D. J. & Hamilton, J. C. First-principles study of the solubility, diffusion, and clustering of C in Ni. *J. Phys. Rev. B* **68**, 094105 (2003) and references therein.

38. Amara, H., Bichara, C. & Ducastelle, F. Formation of carbon nanostructures on nickel surfaces: A tight-binding grand canonical Monte Carlo study. *Phys. Rev. B* **73**, 113404 (2006).
39. Somers, W. *et al.* Temperature influence on the reactivity of plasma species on a nickel catalyst surface: An atomic scale study. *Catal. Today* **211,** 131-136 (2013).
40. Bussi, G., Donadio, D. & Parrinello, M. Canonical sampling through velocity-rescaling. *J. Chem. Phys*. **126,** 014101 (2007).
41. Smith,F. &,Van Cleve, J.W. A Reinvestigation of the Preparation of β-Methyl Lactoside. *J. Am. Chem. Soc.*, **74**, 1912-1913 (1952).
42. Rotzoll, G. High-temperature pyrolysis of ethanol. *Journal of Analytical and Applied Pyrolysis* **9**, 43-52 (1985).
43. Saito, K., Kakumoto, T., Nakanishi, Y. & Imamura, A. Thermal Decomposition of Formaldehyde at High Temperature. *J. Phys. Chem*. **89**, 3109-3113 (1985).
44. Kresse, G., & Furthmüller, J. Efficient iterative schemes for ab initio total-energy calculations using a plane-wave basis set. *Physical Review B*, **54**, 11169 (1996).
45. Hammer, B., Hansen, L., & Nørskov, J. Improved adsorption energetics within density-functional theory using revised Perdew-Burke-Ernzerhof functionals. *Physical Review B*, **59**, 7413–7421 (1999).
46. Kresse, G., & Joubert, D. From ultrasoft pseudopotentials to the projector augmented-wave method. *Physical Review B*, **59**, 1758 (1999).
47. Methfessel, M., & Paxton, A. T. High-precision sampling for Brillouin-zone integration in metals. *Physical Review B*, **40**, 3616–3621 (1989).
48. Ding, F., Rosén, A. & Bolton, K. Molecular dynamics study of the catalyst particle size dependence on carbon nanotube growth. *Chem. Phys.* **121,** 2775–2779 (2004).
49. Henkelman, G., Uberuage, B. P. & Jonsson, H. A. Climbing Image Nudged Elastic Band Method for Finding Saddle Points and Minimum Energy Paths. *J. Chem. Phys*. **113**, 9901-9904 (2000).
50. Hodgson, A. & Haq, S. Water adsorption and the wetting of metal surfaces. *Surface Science Reports* **64**, 381-451 (2009).
51. Benndorf, C & Madey, T. E. Adsorption of H_2O on clean and oxygen-predosed Ni (110). *Surface Science* **194**, 63-91 (1988).
52. Mohsenzadeh, A., Bolton, K. & Richards, T. DFT study of the adsorption and dissociation of water on Ni(111), Ni(110) and Ni(100) surfaces. *Surface Science* **627**, 1-10 (2014).

53. Li, Y., Ahuja, R. & Larsson, J. A. Communication: Origin of the difference between carbon nanotube armchair and zigzag ends. *J. Chem. Phys*. **140**, 091102 (2014).
54. Rao, F.-B., Li, T. & Wang, Y.-L. Effect of hydrogen on the growth of single-walled carbon nanotubes by thermal chemical vapor deposition. *Physica E* **40,** 779-784 (2008).
55. Khalilov, U., Bogaerts, A., Xu, B., Kato, T., Kaneko, T. & Neyts, E. C. How the alignment of adsorbed *ortho* H pairs determines the onset of selective carbon nanotube etching. *Nanoscale*, **9**, 1653-1661 (2017).
56. Ding, F., Jiao, K., Lin, Y. & Yakobson, B. I. How Evaporating Carbon nanotubes Retain Their Perfection? *Nano Lett*. **7**, 681-684 (2007).
57. Malesevic, A., Vizireanu, S., Kemps, R., Vanhulsel, A., Van Haesendonck, C. & Dinescu, G. Combined growth of carbon nanotubes and carbon nanowalls by plasma-enhanced chemical vapor deposition. *Carbon* **45** 2932 (2007).
58. Iijima, S. Growth Model for Carbon Nanotubes. *Phys. Rev. Lett*. **69**, 3100-3103 (1992).
59. He, M., Magnin, Y., Jiang, H., Amara, H., Kauppinen, E. I., Loiseau, A. & Bichara, C. Growth Modes and Chiral Selectivity of Single-walled Carbon Nanotubes. *Nanoscale* **10**, 6744-6750 (2018).
60. Zhang, L., He, M., Hansen, T. W., Kling, J., Jiang, H., Kauppinen, E. I., Loiseau, A. & Wagner, J. B. Growth Termination and Multiple Nucleation of Single-Wall Carbon Nanotubes Evidenced by *In Situ* Transmission Electron Microscopy. *ACS Nano* **11**, 4483-4493 (2017).